Experimental Study on Surface Deterioration Disease of Stone Artifacts Based on Infrared Thermography

Yongguo Chen[1], Zhiwei Pan[1], Liang Ye[1,*], Chengze Ye[2], Jiali Wu[3] and Qing Zhang[3]

[1]School of Civil Engineering and Architecture, Zhejiang University of Science and Technology, Hangzhou 310023, China
[2]International Campus, Zhejiang University, Haining 314499, China
[3]Huagang Management Office of Hangzhou West Lake Scenic Area, Hangzhou 310000, China

_____

Abstract

To accurately identify the deterioration degree of the surfaces of stone cultural relics and determine how various diseases affect each other, the deterioration research combined with infrared thermography and ultrasonic technology was used to effectively detect the deterioration and current situation of the internal structure of rocks and investigate the different states of limestone specimens. The temperature change laws of surface heating and cooling were examined using the distribution of heat and the conduction phenomenon. Infrared thermography was applied to detect the surface deterioration of stone cultural relics and disease development. Results show the limestone specimen surface's temperature change rule during heating and cooling. During the aging process of the limestone specimen, the original disease area deteriorates faster and more seriously than the fresh and unweathered area. The 3D map of the temperature distribution processed by infrared thermography can be used to quickly determine the disease area and semi-quantitatively measure the degree of disease development, which is essential to the protection of cultural relics. The obtained conclusions in this study can provide the reference for the protect of stone cultural relics.

Keywords: Deterioration disease, Infrared thermography, Ultrasonic detection, Temperature variation, Thermal conductivity

_____

1. Introduction

Stone cultural relics, including stone tools, murals, and caves, are historical artistic elements left behind by the human development process. The prevention of irreversible damage to cultural relics is the core of the research on cultural relics. Cultural relic detection and repair aim to protect the original historical appearance of relics as much as possible and reduce the effects of deterioration on them [1]. Ultrasonic detection, infrared thermography, X-ray diffraction (XRD), scanning electron microscopy (SEM), energy spectroscopy, and other methods are increasingly being used to detect the diseases of stone cultural relics [2, 3]. Among them, infrared thermal imaging has been quite popular in recent years due to its strong intuition, simple operation, remote, non-contact detection non-destruction of cultural relics, and other advantages.

At present, infrared thermal imaging technology has been widely used in various industries, and Sweden first began to use infrared thermal imaging technology to detect the energy-saving thermal insulation performance of buildings in 1966. Infrared thermography can be applied to the detection of a variety of diseases in stone artifacts. For the hollow drum disease, the traditional experience of the knocking detection method is not only time-consuming and labor-intensive, but also the detection results are not accurate enough. The infrared thermography method will be based on the difference in thermal conductivity of the hollow drum parts, and more intuitively and accurately show the diseased parts [4, 5]. For the leakage disease, most of the direct observation methods to determine the seepage parts and the

scope of water damage, supplemented by ultrasonic, microwave humidity meter detection to find the source of seepage, but the stone cultural relics due to the age of a long time, the surface of the weathering of the surface of the serious flatness is poor, the signal probe is often difficult to find a smooth plane for detection, so the results will be a large error. Infrared thermography can be remote contactless detection [6]. For the stone cultural relics surface or internal fissures, a variety of existing detection methods can be more accurate to locate its length, width, and general location, but for the detection of the depth of the fissures, often through the secondary development of infrared thermography for assessment [7, 8].

In this study, through the preliminary literature review, combing the use of infrared thermography to detect the status of disease, research infrared thermography to detect stone cultural relics disease deterioration of the rule of law; according to the specification test limestone specimens in different weathering state of a number of mechanical properties indicators, compared to the specimen before and after heating or cooling of different weathering state of the temperature change, to derive the law; the field through ultrasonic determination of stone cultural relics weathering degree, through ultrasound and other conventional means of detection, and then use infrared thermography to detect the surface lesions of stone cultural relics in different weathering degree of heating or cooling before and after the temperature change rule. Infrared thermography detection technology plays an important

role in the protection and inheritance of stone cultural relics.

_____

2. State of the art

In recent studies, infrared thermography has been mainly used to detect the presence of lesions on walls. For example, the difficulty of detecting lesions appearing on the concave and convex surfaces of frescoes in Italian churches has been overcome using IR NDT and 3D data filtering techniques [9]. Kordatos et al. [10] detected frescoes in Greek monasteries with the help of infrared thermography and compared the effects of the different types of lesions by using polymorphic excitation infrared detection techniques. Grinzato et al. [11] detected the sub-surface stratification of gypsum in frescoes in Italian restoration works using transient thermal NDE methods and suggested that thermal modeling can well explain the characteristics of disease evolution. It can be seen that infrared thermography can be well applied to the non-destructive testing of the surface of cultural relics, and it is also effective in detecting the development of internal lesions of cultural relics.

Some other scholars have also studied infrared thermography to detect defects in the internal structure of concrete. For example, Clark et al. [12] used infrared detection technology to detect delamination defects in concrete bridges by using infrared detection technology under low-temperature conditions and achieved good results. Lerma et al. [13] accurately revealed different types of defects caused by construction, environmental, and other factors by comparing real photographs and infrared thermography inspection results of concrete walls in a Spanish college. Rocha et al. [14] evaluated the ability of different types of concrete to delaminate in sunlight using infrared thermography and inserted polystyrene sheets of different thicknesses and depths to simulate defects within the concrete and to assess the ability of infrared thermography to detect these defects. Ishikawa et al. [15] investigated the performance metrics of concrete under non-destructive testing conditions by infrared thermography and examined weathering effects caused by composition and surface discoloration. This shows that the applicability of detecting defects in the internal structure of concrete by infrared detection technology is very strong, which further proves that it is suitable for detecting diseases on the surface of stone artifacts and reduces the damage to the artifacts.

In the field of civil engineering, infrared thermography is mostly applied to the detection of internal cracks in concrete, structural defects, wall bulging detection, etc., while the research and application for stone cultural relics disease and restoration are relatively few. Some scholars used ultrasonic detection and the Carsten bottle method to analyze the cavity development and leakage of stone cultural relics, and only a few scholars applied infrared thermography to this field [16-19]. Therefore, in this study, given the current situation that different surface lesions of stone cultural relics interact with each other, we use infrared thermography to study the heat distribution and conduction laws of different lesions and propose a method for evaluating the deterioration of surface lesions of stone cultural relics based on infrared thermography [20-22], which is crucial for the monitoring and protection of the structural health of stone cultural relics and is of practical application value [23-25].

The rest of this study is organized as follows. Section 3 gives the relevant methodology. Section 4 presents the results analysis and discussion, and finally, the conclusions are summarized in Section 5.

3. Methodology

3.1 Sample preparation

Stone cultural relics are national culture bearers. They are the accumulation of a nation's history, the crystallization of civilization, and a witness to human civilization. Stone cultural relics are spectacular, but after thousands of years of rain and wind, they suffer from many diseases, the most common of which are leakage, fissure, and hollow drum disease. Many scholars have conducted research on a single disease, but how to examine various diseases simultaneously while keeping in mind the protection of stone cultural relics is essential [26, 27]. The simulation of different moisture contents and weathering degrees under various conditions can serve as a basis for infrared thermal imaging detection of diseases, analysis of the temperature change law of field test data, and quantitative investigation of heritage surface disease development [28, 29].

The selected test material was limestone with the same material as the stone cultural relics near Baifo Rock in Wushan Scenic Area, Hangzhou City, Zhejiang Province. Limestone's structure is dense, crystalline granular, bioclastic, and brittle, and it is characterized by chemical reactions that produce gas bubbles in the presence of dilute hydrochloric acid. The specimens used in this study were limestone rectangular blocks with dimensions of 100 mm × 100 mm × 100 mm. Two square blocks were cut and coded as A and B. Fissures that were 1-5 mm deep were scribed on each of the five surfaces of Block A, and fissures that were 6-10 mm deep were scribed on each of the five surfaces of Block B. The specimens are shown in Fig. 1.
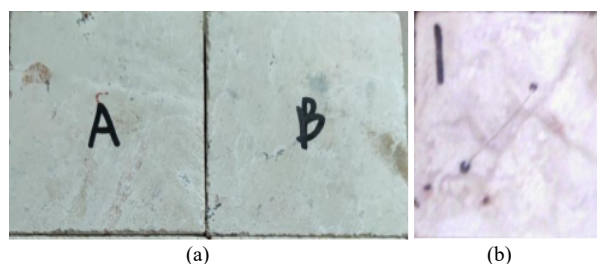

(a)   (b)
Fig. 1. Slit specimen. (a) Test block number. (b) Fissure plane.

Finding a suitable test block in the stone cultural relics with the hollowing disease formed over the years by weathering in the Wushan Scenic Area near Hundred Buddha Rock in Hangzhou City, Zhejiang Province, was difficult. Stone cultural relics that are commonly used in lime-based slurry were selected for specimen preparation to analyze the damage and shedding caused by the hollowing disease and explore the same depth in the same area and the same area with the same depth of hollowing caused by the law of the difference in temperatures [30-32]. This slurry is composed of $CaCO_3$. The Hundred Buddhas Rock before the dislodgement of the broken pieces of the X-ray diffractometer and the results of heat loss from the gravity test are shown in Fig. 2.

The XRD spectra in Fig. 2(a) show calcite absorption peaks and a few SiO_2 absorption peaks, indicating that the sample consisted of $CaCO_3$ and SiO_2. The heat loss test, which is a quantitative test method, was applied to the sample. Analysis of the thermogravimetry (TG) curve in Fig. 2(b) indicates that a mass loss occurred only between 600 °C and 900 °C, and this process was the thermal decomposition of calcium carbonate. The heat loss weight of the Baifo rock

sample was 41.8%, and the calcium carbonate content was calculated to be 95%. The sample contained a few impurity components. According to the XRD results, the impurity components were SiO_2 and bioclastic debris, and the total content of the impurities was less than 5%. As shown in Fig. 3, the test blocks were prepared at a water–cement ratio of 1:5, and after the preparation, molds with different sizes of concave areas were set up and filled with beeswax, followed by a layer of 2-mm-thick mortar to cover them. Fig. 3(a) shows different hollows with the same area and depth, and Fig. 3(b) presents different hollows with varying areas and depths.

(a)

(b)
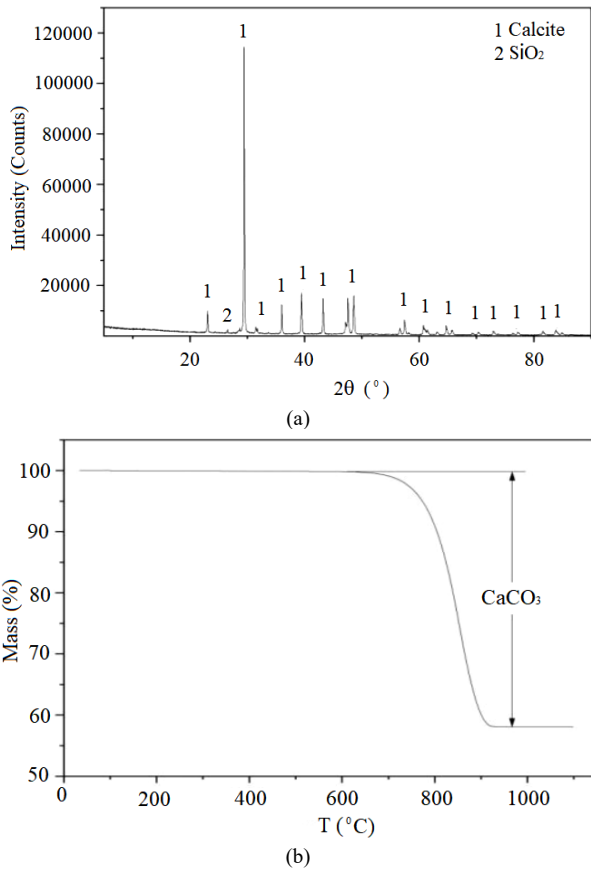
Fig. 2. Compositional assay of Baifo rock samples. (a) XRD spectrum. (b) TG curve.

This test adopted the active infrared detection method to closely observe the changes in the surface temperature of the test block. The external heat source was a Philips infrared dry baking lamp with a bulb power of 375 W, the maximum temperature of 60 °C, a wavelength range of 0.76-5 μm, and a peak wavelength of 4 μm [33].
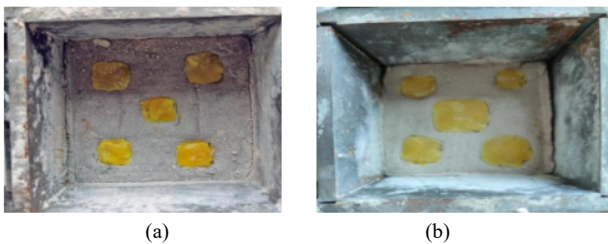

| (a) | (b) |

Fig. 3. Cavitation test block fabrication. (a) Drums of the same size and depth. (b) Drums of varying sizes and depths

3.2 Experimental procedure

3.2.1 Archimedes drainage
A suitable size of the specimen was obtained, the initial mass was weighed, and the specimen was placed in a 60 °C drying oven for 8 h (the time varied in accordance with the size of the sample). The specimen was dried to a constant weight and then cooled at room temperature for 1 h. Afterward, its mass was weighed again. The treated specimen was submerged in a container filled with deionized water and placed in a vacuum drying oven for at least 1 h to discharge the air in the pores of the specimen. Immediately after removing the specimen, the surface of the specimen block was wiped with a wrung-out wet towel, and the mass of the specimen was weighed after water absorption and saturation. Then, the mass of the specimen in water was weighed.

3.2.2 Scanning electron microscope images
The morphology of the samples was characterized using a Hitachi S-4700 scanning electron microscope, as shown in Fig. 4, where (a) is the SEM image of the fresh specimen block sample, (b) is the SEM image of the slightly weathered specimen block sample, and (c) is the SEM image of the moderately weathered specimen block sample.
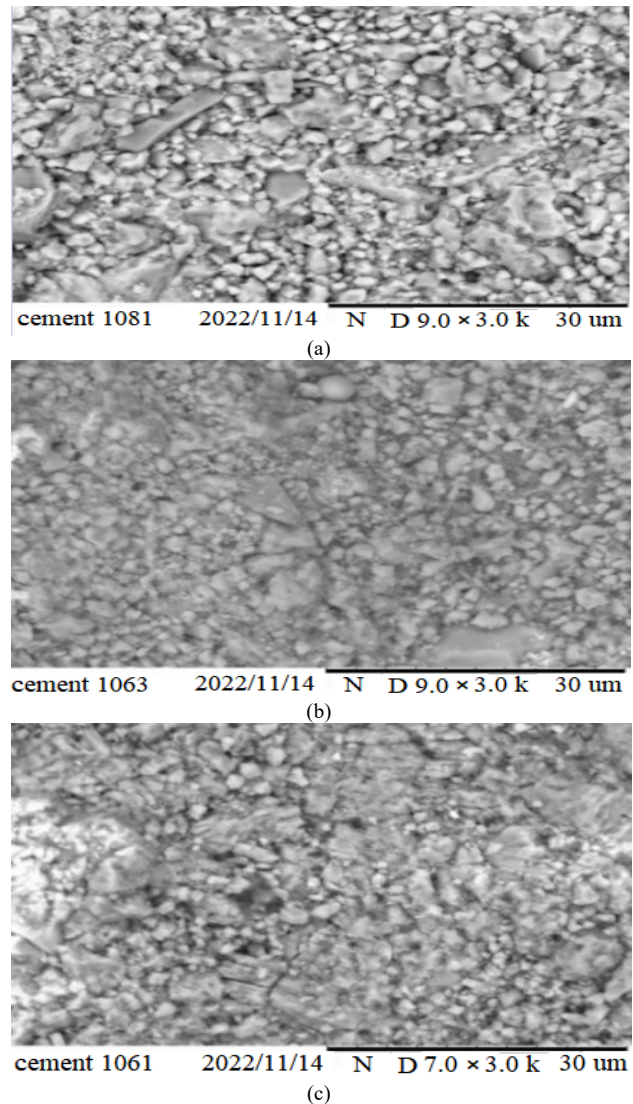

cement 1081   2022/11/14   N D 9.0 × 3.0 k   30 um

(a)

cement 1063   2022/11/14   N D 9.0 × 3.0 k   30 um

(b)

cement 1061   2022/11/14   N D 7.0 × 3.0 k   30 um

(c)

Fig. 4. Scanning electron microscope (3,000×) results. (a) Diagram of fresh test block samples. (b) Diagram of a sample of micro-weathered specimens. (c) Diagram of a sample of medium-weathered specimens.

3.2.3 Threshold-based Photoshop image segmentation method

As shown in Fig. 5, in accordance with the porosity of the sample derived from the Archimedes drainage method, the corresponding SEM image of the sample was substituted into Photoshop calculation, and the image was binarized by continuously adjusting the threshold value in the interval of 0-256. The image was converted into a black-and-white binary image, in which black represents the pore space. The porosity results close to that of the drainage method was calculated using the ratio of the black and white elements. Fig. 5(a) shows the fresh sample at a threshold of 108, Fig. 5(b) shows the slightly weathered sample at a threshold of 108, and Fig. 5(c) shows the moderately weathered sample at a threshold of 108. The results of the porosity comparison are given in Table 1.
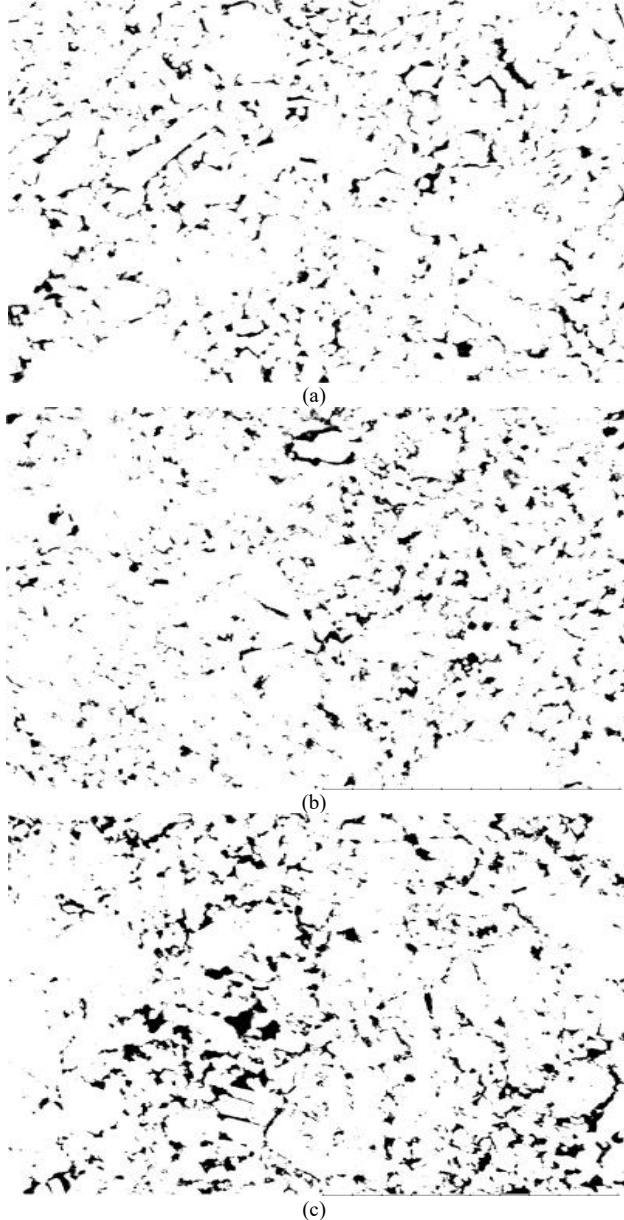

Fig. 5. Black-and-white binary image at a threshold of 108. (a) Diagram of fresh test block samples. (b) Diagram of a sample of micro-weathered specimens. (c) Diagram of a sample of medium-weathered specimens.

Table 1. Comparison of porosity results.

Trial blocks	Average value of the open porosity of Specimens A and B	Calculated results at 108 threshold
Fresh condition	2.425 %	2.612 %
After 15 days of alternating	6.285 %	6.094 %
acid and alkali immersion (slightly to moderately weathered state)		
After 30 days of alternating acid and alkaline soaking (medium-strong weathering state)	9.720 %	9.283 %

3.3 Theory test

3.3.1 Ultrasonic testing

The RSM-SY7 acoustic wave detector of Zhongyan Technology was used to detect the internal structure of the stone cultural relics. Ultrasonic testing is usually performed based on the characteristics of sound waves in different media with different propagation speeds to determine the internal density of the rock via nondestructive testing means, and it detects the development of comprehensive leakage, fissures, drums, and other surface weathering diseases before judging the surface weathering degree of the rock. In the results of infrared thermal images, dividing the weathering grade on the surface of stone cultural relics is therefore important [34].

Given that the total volume of the acoustic detector and receiver volume was relatively larger than the test block's volume, the overall area could not be subdivided into areas for detection. The flat test method was employed to determine the surface area of the test block. The method was implemented in accordance with the engineering specification (WW/T 0063-2015) of the acoustic rock test method for stone cultural relic protection. The two transducers were placed at a certain distance, and the coupler was fixed on the rock surface to be tested. The distance between the midpoints of the two transducers was measured, and this value was the distance of sound wave propagation in the rock. When the acoustic wave instrument was started, the time scale value corresponding to the first jumping point of the waveform curve displayed on the fluorescent screen was adopted as the time of arrival of the longitudinal wave (t_p).

The longitudinal wave speed was calculated Eq. (1) follows:

$$V_p = \frac{S}{t_p - t_0} \tag{1}$$

where V_p is the velocity of the longitudinal wave (m/s). S is the distance of acoustic wave propagation (m). t_p is the arrival time of the longitudinal wave (μs). t_0 is the zero error of instrument system (μs).

In accordance with the China Code of Practice for the Investigation of Conservation Works for Stony Cultural Relics and on the basis of experience in engineering geology, the degree of weathering of rocks is quantitatively described by rock weathering coefficient F_S, The longitudinal wave speed was calculated Eq. (2) follows:

$$F_S = \frac{V_{p_0} - V_p}{V_p} \tag{2}$$

where F_S is the rock weathering coefficient. V_{p_0} is the fresh rock's longitudinal wave velocity (m/s).

The specific evaluation and grading requirements are as follows: $F_S < 0.1$ for unweathered, $0.1 \leq F_S < 0.25$ for slightly weathered, $0.25 \leq F_S < 0.5$ for weakly weathered, and $F_S \geq 0.5$ for strongly weathered.

3.3.2 Hardness test

The surface hardness of the specimen was tested using the SHENDAWEI SW-6210 Richter hardness tester. The weathering area of the rock surface had high porosity, so its strength and hardness were reduced. The surface of the stone artifacts was tested using the Richter hardness tester, and the ratio of the average hardness value of the weathered area to the average hardness value of the fresh rock samples was adopted to evaluate the degree of weathering of the stone artifacts.

As shown in Fig. 6, the surface of the specimen was divided into three areas (around the fissure, intermediate area, and edge of the surface to be detected) to determine the surface hardness of the specimen under different degrees of weathering. Ten values were measured and read in each area, and the largest and smallest values were removed to obtain the average value.

Fig. 6. Rock samples from Hundred Buddhas Rock.

3.3.3 Water absorption test

The MS310 moisture meter was used to test the water absorption of the surface of the stone artifacts. The moisture meter was adopted before sprinkling. Two times of sprinkling were performed, and the interval was 10 min. Before and after sprinkling, the water content increased rapidly, indicating that the surface of the stone body was loose, and the degree of weathering of the stone was high [35].

The surface of the specimen was divided into three areas (around the fissures, intermediate area, and edge of the surface for testing) to determine the water absorption rate of the surface of the specimen under different degrees of weathering. Ten values were read in each area, and the maximum and minimum values were removed to obtain the average value.

3.4 Detection of the temperature change on the test block surface

3.4.1 Heating program

These specimens are fresh rocks as they were cut from the hills near the lithics. Two rocks were placed in a desiccator to dry and cooled at room temperature. After the surface temperature of the specimens had stabilized, each cracked surface was placed under an infrared heat lamp and heated at a maximum temperature of 60 °C for 30 minutes. Then, the temperature of the heated surface was read with an infrared

thermographic camera. After testing 10 specimens with cracked surfaces, rocks A and B were immersed in water and the heating step was repeated in a dry state in order to detect the temperature change of their surfaces at 10% and 12% water content [36].

Given that Hangzhou experiences acid rain, which is mainly composed of sulfuric acid, all year round, the two test pieces (A and B) were placed in a sulfuric acid solution for aging simulation. Fifteen days after the pieces were taken out of the solution, their surface states reached the micro–medium weathering stage. The process of detecting the fresh states of A and B was repeated with the infrared thermal imaging camera to examine the micro-weathering stage and water content on the surface and the different changes in temperature after heating. The temperature change after heating was read by infrared thermography. Subsequently, test pieces A and B were placed in a hydrochloric acid solution for aging simulation and taken out after 15 days. The surface condition was measured and found to have reached the stage of medium–strong weathering. The testing process for the test pieces at the stage of micro–medium weathering was repeated.

Given that the heating area of the infrared heating lamp was circular, each defect in the hollow test pieces could not be heated uniformly. Therefore, the drying box was used as a heating source instead of the infrared heating lamp. The two test pieces were placed in the drying box, dried to a dry state, and cooled to room temperature. The drying box's temperature was set to the same temperature as the infrared heating lamp temperature of 60 °C. Heating was performed 30 min after infrared thermography to determine the temperature of the heated surface. The surface porosity of the empty drum test piece for the lime-based grout preparation test was larger than that of natural rock. Hence, if it is soaked in water to change its water content, moisture will easily invade the internal part of the test piece, thus affecting the rule of law of temperature change after heating. Therefore, the experiment used only the test piece at the dry state of heating, and different volumes of the empty drum were adopted to examine the law of heat transfer and the similarities and differences.

3.4.2 Determination of the thermal conductivity of the test pieces

Infrared cameras operate based on the principle that different objects have different thermal conductivities and that the thermal conductivity of the same object varies at different states. The thermal conductivity of rock is related to its mineral composition, internal particle arrangement, porosity, and water content and changes with the surface pressure state and temperature.

The test used the TCM-2 series of thermal conductivity testers, and a computer was employed to achieve fully automated detection. The temperature of the hot surface on the hot side was stable, and the heat was transferred through the sample to the cold side. The heat flow of the transfer was measured, and on the basis of the thickness of the specimen and the area of heat transfer, the coefficients of thermal conductivity and thermal resistance were calculated. The main technical specifications of the instrument were as follows: thermal conductivity range of 0.015–5 W/mk for plate-like samples and 3-500 W/mk for cylindrical samples and heat flow range of 0.5-2000 W/m². A WPY heat flow meter with a heat flow parameter of 23.26 w/m² × mV was utilized.

As shown in Tables 2 and 3, with the increase in the porosity and water content of the test block, its thermal conductivity decreased because the internal pores of the test block were full of air in the dry state, and the air thermal conductivity was only 0.0267 W·m^{-1}·K^{-1}. However, due to the aging process of the test block being short, only the surface layer of the test block to the shallow depth of porosity showed an obvious reduction. The test block was still fresh, and the rock particle structure arrangement was dense. Thus, for the rock sample as a whole, the decrease in the tester's detected thermal conductivity was small. Notably, the infrared camera only detected the temperature of the object at the shallow layer, so for the test block, only the change in porosity at the surface layer was in line with the test requirements of the infrared thermal imaging camera.

Table 2. Thermal conductivity test data of Test Block A.

Degree of weathering of rock samples (porosity)	Rock sample water content	Thermal conductivity / (W·m^{-1}·K^{-1})		
		Minimum value	Maximum value	Mean value
Fresh state (2.44%)	0% (dry state)	3.66	4.01	3.82
Fresh state (2.44%)	1.6% (water-saturated state)	3.62	3.99	3.81
Slightly–moderately weathered condition (6.29%)	0% (dry state)	3.57	3.98	3.73
Slightly–moderately weathered condition (6.29%)	1.6% (water-saturated state)	3.57	3.95	3.71
Moderately–strongly weathered condition (9.68%)	0% (dry state)	3.53	3.84	3.66
Moderately–strongly weathered condition (9.68%)	1.6% (water-saturated state)	3.50	3.81	3.62

Table 3. Thermal conductivity test data of Test Block B.

Degree of weathering of rock samples (porosity)	Rock sample water content	Thermal conductivity / (W·m^{-1}·K^{-1})		
		Minimum value	Minimum value	Minimum value
Fresh state (2.41%)	0% (dry state)	3.67	4.06	3.85
Fresh state (2.41%)	1.6% (water-saturated state)	3.63	4.02	3.83
Slightly–moderately weathered condition (6.38%)	0% (dry state)	3.55	4.00	3.72
Slightly–moderately weathered state (6.38%)	1.6% (water-saturated state)	3.53	4.01	3.71
Moderately–strongly weathered condition (9.71%)	0% (dry state)	3.49	3.82	3.64
Moderately–strongly weathered condition (9.71%)	1.6% (water-saturated state)	3.49	3.81	3.63

4. Results analysis and discussion

4.1 Research on the ultrasonic detection mechanism
The results of ultrasonic testing by specialized machines are shown in Table 4.

Table 4. Ultrasonic detection results.

Test blocks	Longitudinal wave speed (m/s)	Weathering factor F_S
Fresh specimen	4,287	0.05
Slightly weathered specimen	3,091	0.46
Strongly weathered test pieces	2,166	1.08

The longitudinal wave velocity in all the detected areas was the average of 30 sets of values. The longitudinal wave velocity of the reference fresh rock was about 4,000–5,000 m/s. As shown in Fig. 6, the average value of the longitudinal wave velocity of the selected rock of the same material on Ziyang Mountain after bringing it back to the laboratory to cut off the weathering layer on the surface and then reading it via ultrasound for 30 times was about 4,500 m/s.

4.2 Hardness values and water absorption results
As indicated in Fig. 7, the surface hardness value of the fresh specimen was between 700 and 720, and the difference between the three tested areas was small. The test piece after acid–alkali aging reached the state of slightly weathered. The hardness of zone 1 and zone 2 on the surface of the test block decreased sharply, and the average hardness value decreased by 191.78 and 202.59, respectively. The hardness value of Area 3 also declined considerably, showing an average decrease of 153.22, which is smaller than the average decrement value for the two other areas. When the test block reached the state of moderately weathered, the decline in the hardness of Areas 1 and 2 areas slowed down, and the average values were 34.97 and 33.44, respectively. At this time, the hardness of Area 3 still exhibited a small decline, and the average value was only 11.12. In the state of weathering, the surface hardness of the test block generally exhibited the following: the deeper the depth of the fissure was, the lower the hardness of the surrounding area was. The existence of fissures on the rock surface intensified the weathering process from the fissures to the two sides of the rock, and for the rocks without fissures on the intact surface, weathering began on the edges of the corners and eroded to the middle of the rock.
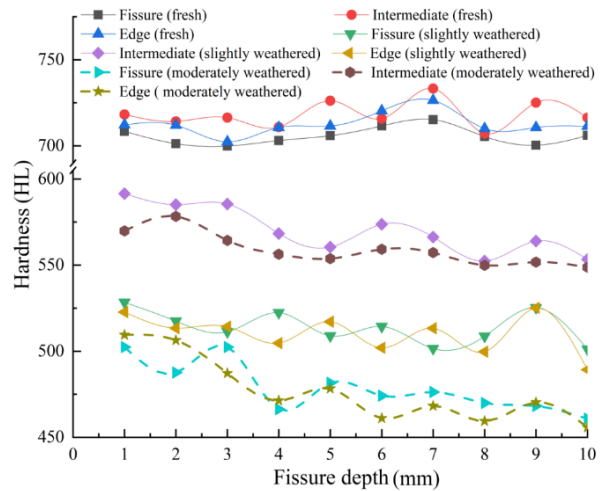

Fig. 7. Surface hardness of test pieces with different degrees of weathering

As indicated in Fig. 8, the overall law of limestone water absorption was as follows: the higher the weathering degree of the test block was, the deeper the fissures were on the surface of the test block and the greater the change was in water content before and after sprinkling water on the surface of the test block. The content change near the fissure on both sides of the water was the largest because after sprinkling water, the fissure was easily attached, and the fissure at the rock material became increasingly loose. Thus, the water easily spread and was stored from the fissure to the internal pores of the rock body.
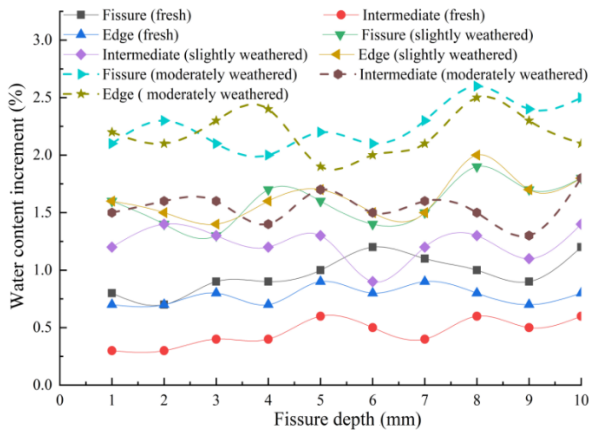
Fig. 8. Surface water absorption of test blocks with different degrees of weathering.

4.3 Infrared detection of the surface temperature of the test block and changes in its value

4.3.1 Infrared thermal image processing analysis
The FOTRIC 326Q handheld infrared camera was used for this test, and the images were imported into the software AnalyzIR for image processing [37, 38].
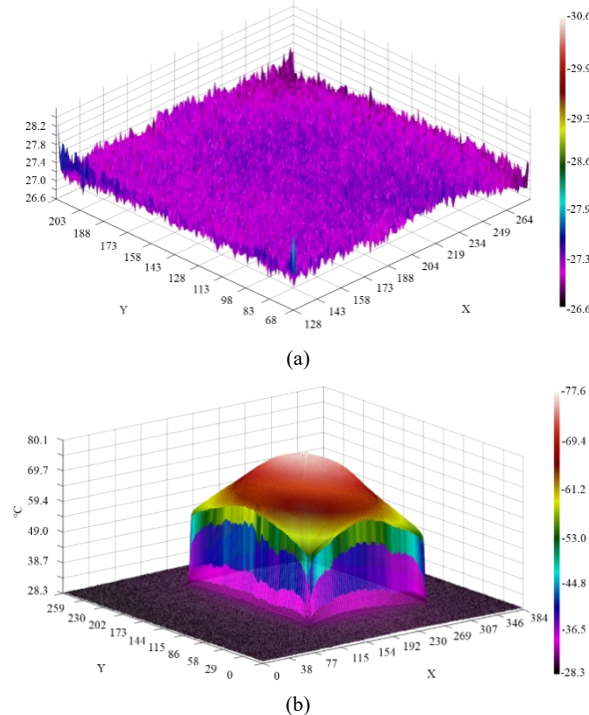

(a)

(b)

Fig. 9. 3D graph of temperature distribution on the surface of the specimen. (a) Before heating. (b) After heating.

As seen from Fig. 9, the color distribution of the representative temperature was uniform, and the color difference was small, indicating that the surface temperature of the test block was uniformly distributed before heating. After the test piece was heated, the color area representing the temperature in the middle of the test piece exhibited obvious bulging. This situation, combined with the example of the temperature distribution on the right side of the graph, shows that the temperature of the surface of the test piece at this time decreased from the middle of the fissure to the two sides. That is, the closer the location was to the fissure, the larger the increase in temperature was; the increase in temperature at the fissure was the largest among all the increments [39].

(a) (b)
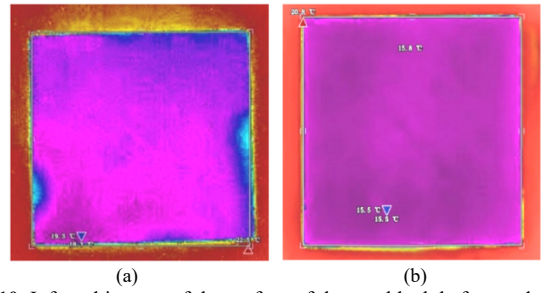
Fig. 10. Infrared images of the surface of the test block before and after cooling. (a) Before cooling. (b) After cooling.

Fig. 10 shows that the surface temperature distribution of the specimen before and after cooling was uniform. A comparison of this figure with Fig. 10 indicates that the location and shape of the fissures after cooling were not as clear as those after heating.
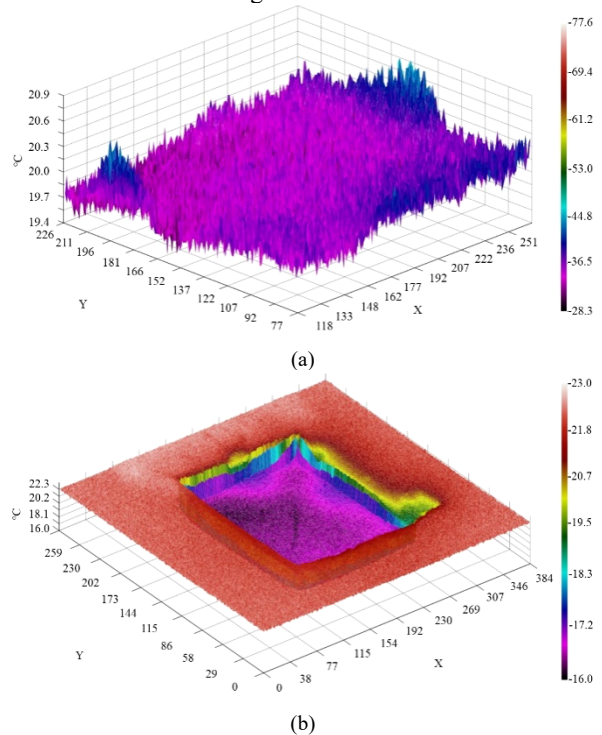

(a)

(b)

Fig. 11. 3D graph of temperature distribution on the surface of the specimen. (a) Before heating. (b) After heating.

Comparative analysis of Fig. 11 showed that the effect of changing the surface temperature of the test object by water spray cooling was minimally effective but still successful overall. During the water spray cooling of the test block's surface, the middle of the colored area of the test block showed that the temperature was reduced. At this time, the test block's surface temperature increased from the middle of the fissure to both sides. The closer the location was to the fissure, the larger the temperature drop was; the fissure at the temperature drop was the largest among all the fissures.

A comparative analysis of Figs. 12 and 13 showed that the empty drum test piece had a low temperature before heating and a high temperature after heating. The distribution of the location of the drum and the shape and size of the drum are visible. Before heating, the beeswax temperature was much higher than the temperature of the test piece, and the temperatures of the different areas with the same depth of the hollow drum test piece varied because the size of the beeswax was not the same. The results of infrared thermography detection were not uniform, indicating that the damage to the hollow drum test piece

with the size of the beeswax and the central beeswax exhibited the same temperature phenomenon as that presented by the test piece.
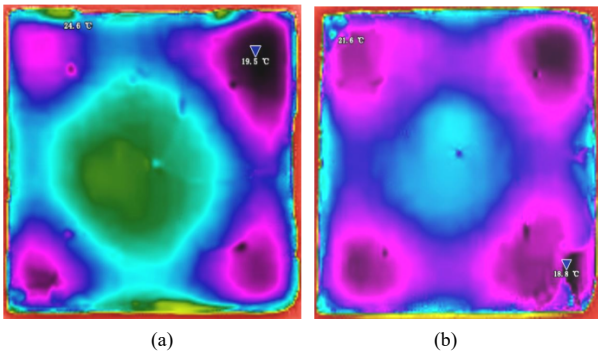

(a)   (b)

Fig. 12. Infrared image of the test piece surface before heating. (a) Different areas with the same depth of the empty drum test piece. (b) Different depths with the same area of the empty drum test piece.
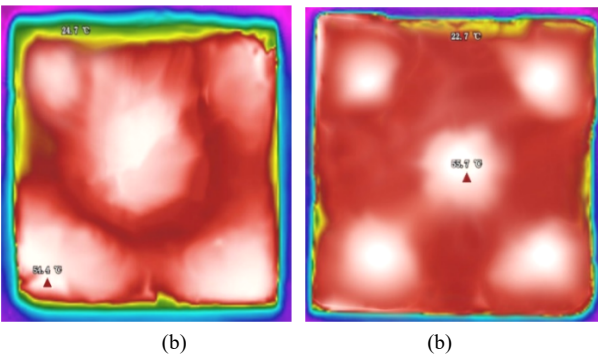

(b)   (b)

Fig. 13. Infrared image of the specimen surface after heating. (a) Different areas with the same depth of the empty drum test piece. (b) Different depths with the same area of the empty drum test piece.

Comparative analysis of Fig. 14 revealed that before heating, the temperature of the colored area in the middle of the test block was reduced. After heating, the temperature of the colored area in the middle of the test block exhibited bulging. The 3D map of the temperature distribution on the rest of the surface of the test block intact area before and after heating presented a small change. This observation, combined with the right side of the temperature distribution of the graphical examples, indicates that the temperature on the surface of the test block with hollowing defects before and after heating increased greatly. In addition, the depth of the internal hollow drum was roughly assessed with the help of the temperature distribution in the 3D map. The results showed that the infrared thermal imaging camera effectively detected the area and depth of the internal hollow drum of the test piece, and the temperature change was large when the area and depth were large.
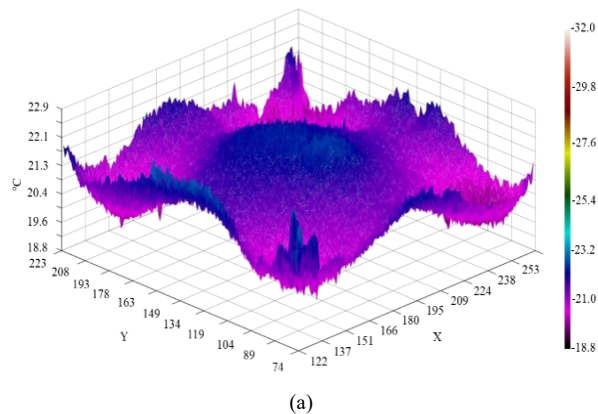

(a)
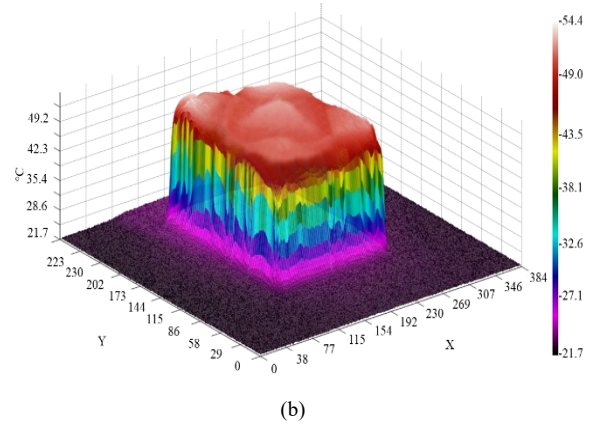
(b)

Fig. 14. 3D graph of temperature distribution on the surface of the specimen. (a) Before heating. (b) After heating.

4.3.2 Results of the numerical calculation of the surface temperature change of fissure lesions

Classification by the degree of weathering of the test block: The analysis of the temperature variation of the specimen before and after heating or cooling (Figs. 15-17) revealed that under the same weathering conditions, the higher the surface water content and the larger the depth of the fissure of the specimen were, the greater the temperature variation was.
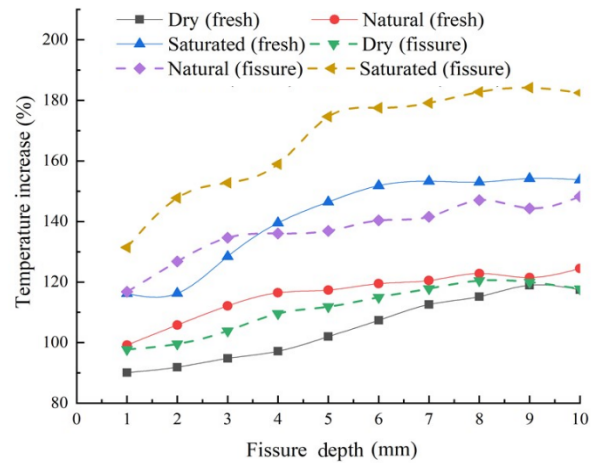
(a)
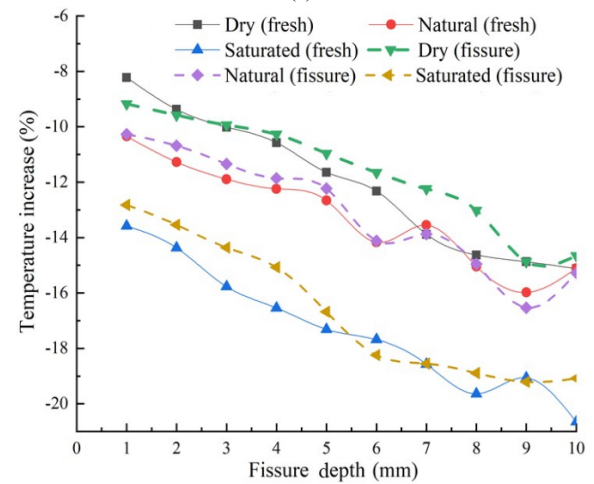
(b)

Fig. 15. Fresh specimen. (a) Temperature increment after heating. (b) Temperature decrement after cooling.

Figs. 16-21 reveal that under the heating condition, the temperature variation at the fissure was much higher than the overall temperature variation at the surface where the fissure was located, and the differentiation of the fissure was more obvious.
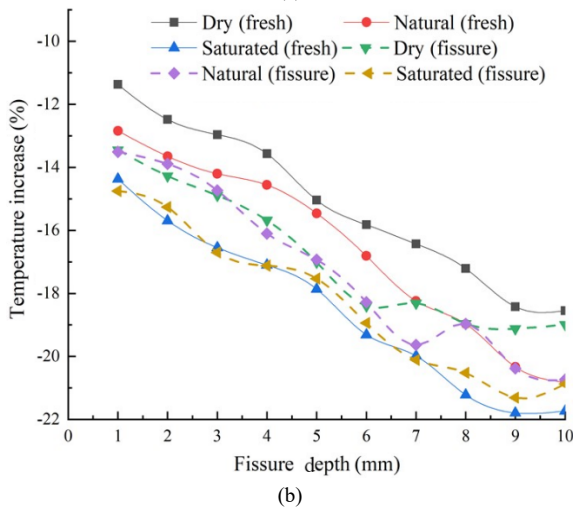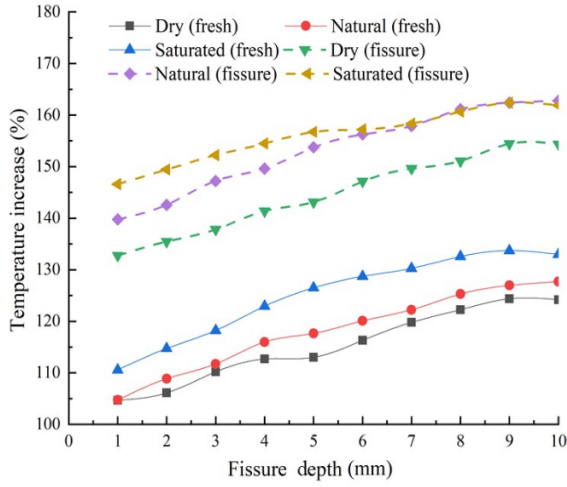

(a)

(b)

Fig. 16. Slightly–moderately weathered specimen. (a) Temperature increment after heating. (b) Temperature decrement after cooling.
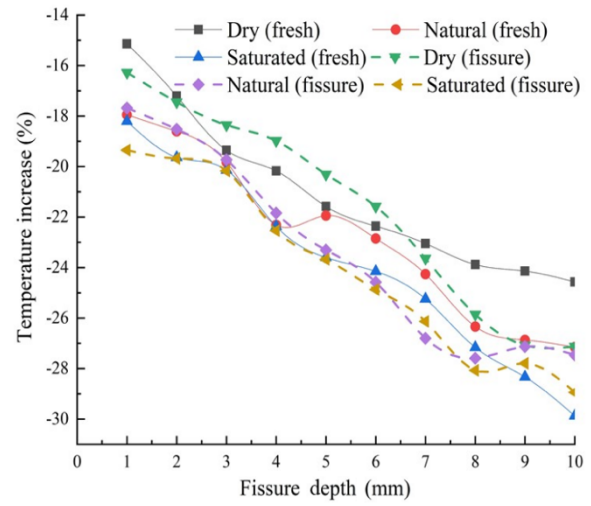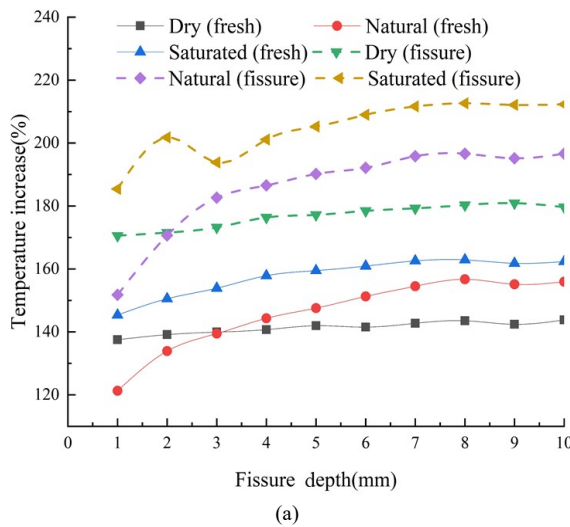

(a)

(b)

Fig. 17. Moderately–strongly weathered specimen. (a) Temperature increment after heating. (b) Temperature decrement after cooling.

Classification by the surface moisture content of the test pieces: Figs. 18-20 show that the higher the surface weathering and the larger the fissure depth of the test block was under the same water content, the greater the magnitude of the temperature change was.
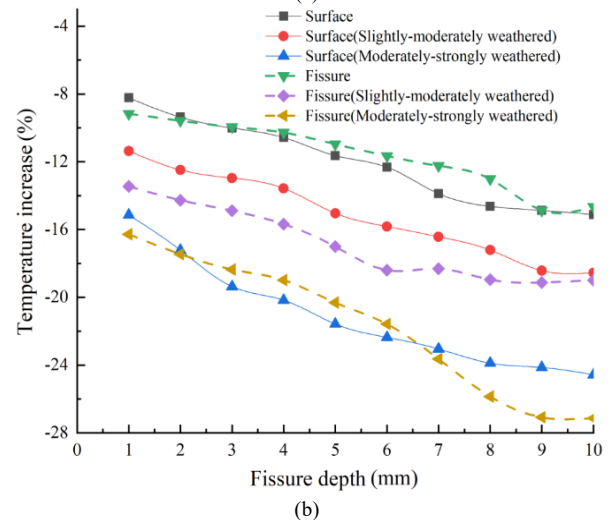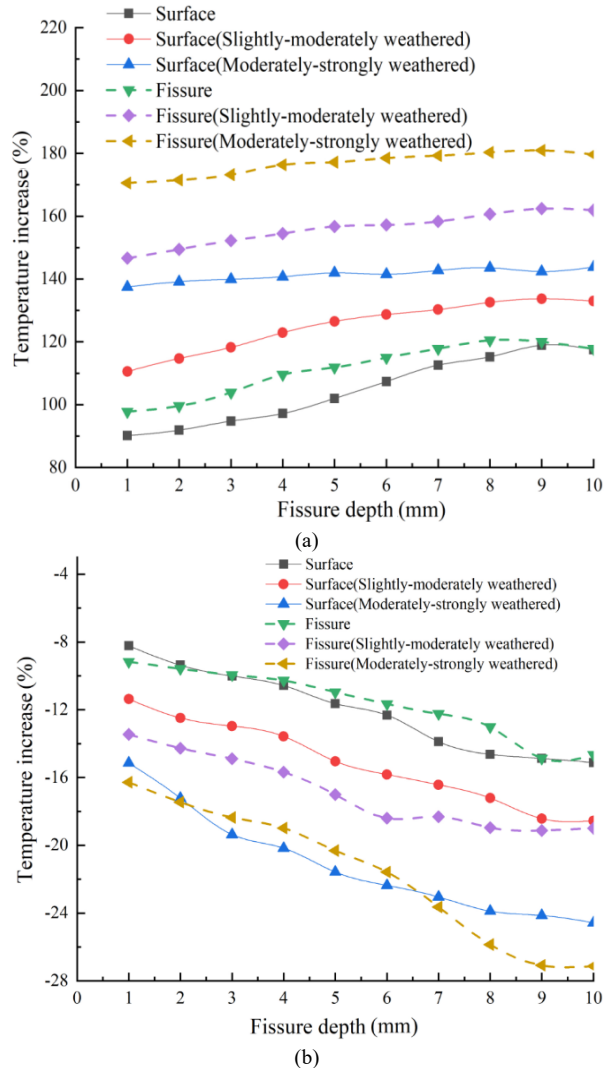

(a)

(b)

Fig. 18. Dry condition (surface moisture content of about 8%). (a) Temperature increment after heating. (b) Temperature decrement after cooling.
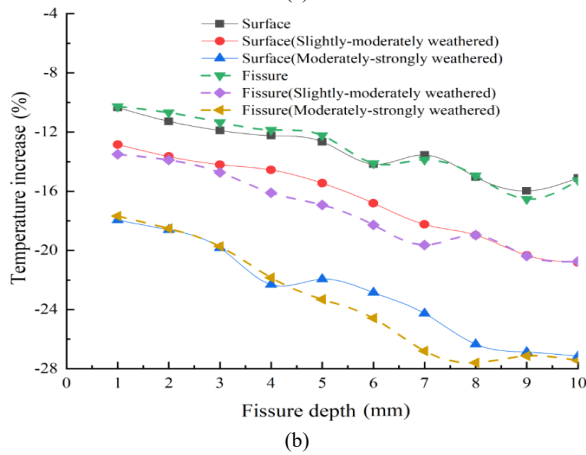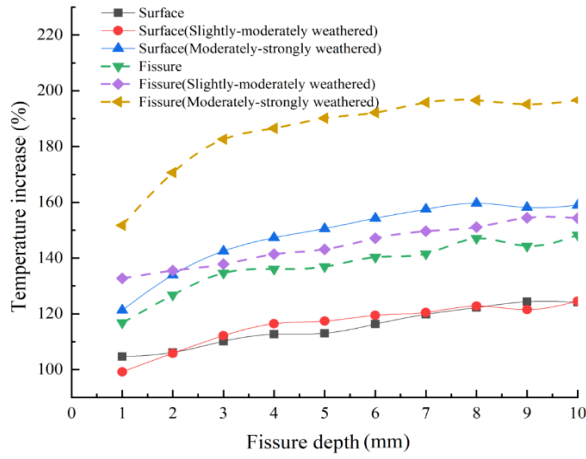
(a)

(b)

Fig. 19. Natural state (surface moisture content of about 10%). (a) Temperature increment after heating. (b) Temperature decrement after cooling.

On the contrary, under the cooling condition, the temperature variation at the fissure was higher than that at the surface where the fissure was located, but the difference was small, and the temperature variations were close to one another. In addition, the line graph flattened out after the depth of the fissure reached 6-7 mm, indicating that the infrared thermal imaging camera had certain limitations in detecting the depth of the disease. These findings reveal the law of heat transfer inside the specimens in different states and indicate that the resulting surface temperature distributions of the specimens were closely related to the water content, fissure depth, and weathering degree of the specimens. These results confirm the feasibility of using infrared thermography to detect the surface deterioration of stone cultural relics.
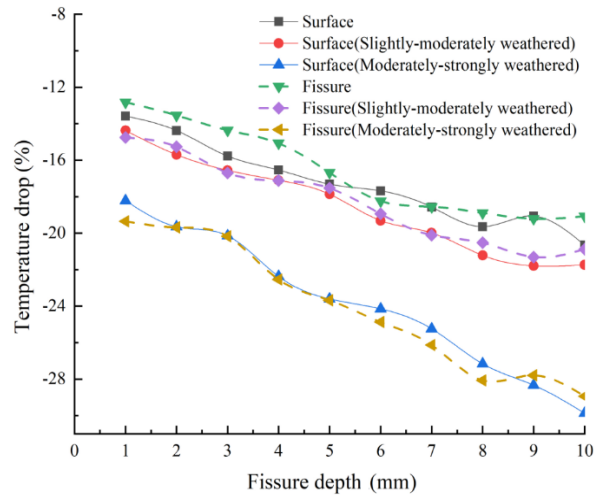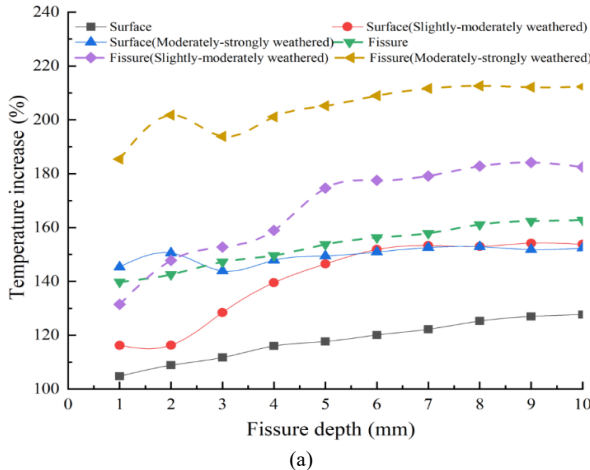

(a)

(b)

Fig. 20. Water-saturated condition (surface moisture content of about 12%). (a) Temperature increment after heating. (b) Temperature decrement after cooling.

4.3.3 Surface temperature change in hollow drum lesions
As indicated in Fig. 21, the larger the depth of the hollow drum was, the larger the area was and the greater the increase in temperature was before and after heating. The size of the hollow drum area and the increment were primary functions. The depth of the hollow drum and the increment presented a class of logarithmic functions that were related to the overall trend of the increment. The infrared detection of the shape, size, and location distribution of the drum produced excellent results.
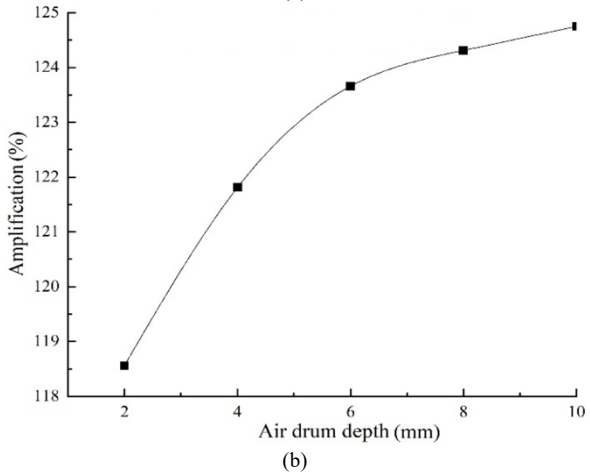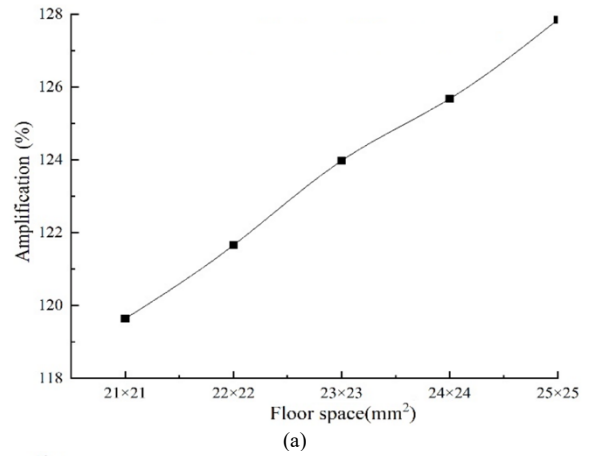

(a)

(b)

Fig. 21. Surface temperature change results of the empty drum specimen. (a) Different areas with the same depth of the hollow drum test piece. (b) Different depths with the same area of the hollow drum test piece.

5. Conclusions

The ultrasonic velocity, water absorption, hardness, and thermal conductivity of the specimens under different degrees of weathering were evaluated through indoor tests. The morphology of the test blocks in different states was characterized via SEM, and the optimal threshold of the black-and-white binary map of the SEM image was back-deduced by Photoshop in accordance with the open porosity measured by the drainage method. Then, the temperature change rule during the heating and cooling the surface of the test block in different states was observed by infrared. The main conclusions were obtained as follows.

(1) The overall deterioration law of the limestone test block during the aging process was as follows: deterioration from the fissure to both sides and deterioration from the edge corner to the middle. Specifically, the original diseased area in the aging process had a higher deterioration speed and more serious deterioration degree than the fresh unweathered area.

(2) After heating and cooling the specimen, the infrared camera found that the higher the weathering degree and moisture content of the specimen were, the greater the temperature variation was before and after heating or cooling the surface of the specimen. The deeper the fissures

and hollow drums were, the larger the area of the hollow drums was, and the greater the temperature variation was.

(3) The pictures obtained by the handheld infrared camera became clear after processing by the supporting software, and the results became increasingly intuitive after they were transformed into a 3D map of temperature distribution. This map is useful for quickly confirming the area where the disease is located and semi-quantitatively quantifying the degree of disease development.

(4) Black-and-white dichotomization was performed on the SEM images of the specimens with different porosities measured by the drainage method to determine the optimal threshold value of 108, which was then used to assess the size of the porosity during the observation of the surface morphology of the artifacts (only rocks of the same type) via field inspection using a portable microscope (500 ×).

_____
References

[1] C. Liu and M. Xu, "Characteristics and influencing factors on the hollowing of traditional villages-Taking 2645 villages from the Chinese traditional village catalogue (Batch 5) as an example," *Int. J. Environ. Res. Public Health*, vol. 18, no. 23, pp. 12759, Dec. 2021.

[2] M. O. Sunnetci and H. Ersoy, "A new perspective based on overcoming sample heterogeneity for the estimation of thermal damage inflicted on volcanic rocks using non-destructive tests," *Rock Mech. Rock Eng.*, vol. 56, no. 1, pp. 35-56, Dec. 2023.

[3] E. Edis, I. Flores-Colen, and J. de Brito, "Passive thermographic detection of moisture problems in façades with adhered ceramic cladding," *Constr. Build. Mater.*, vol. 51, pp. 187-197, Jan. 2014.

[4] C. A. Balaras and A. Argiriou, "Infrared thermography for building diagnostics," *Energy Build.*, vol. 34, no. 2, pp. 171-183, Feb. 2002.

[5] R. Fort, J. Feijoo, M. J. Varas-Muriel, M. Navacerrada, M. Barbero-Barrera, and D. De la Prida, "Appraisal of non-destructive in situ techniques to determine moisture-and salt crystallization-induced damage in dolostones," *J. Build. Eng.*, vol. 53, Aug. 2022, Art. no. 104525.

[6] Z. Qu, P. Jiang, and W. Zhang, "Development and application of infrared thermography non-destructive testing techniques," *Sensors*, vol. 20, no. 14, Jul. 2020, Art. no. 3851.

[7] C. Meola, L. Nele, and L. Giorleo, "Technological characterisation of thermoshrinking cross-linked polyethylene by destructive and non-destructive techniques," *J. Mater. Process. Tech.*, vol. 133, no. 3, pp. 353-358, Feb. 2003.

[8] Q. Li, T. Yin, X. Li, and S. Zhang, "Effects of rapid cooling treatment on heated sandstone: a comparison between water and liquid nitrogen cooling," *Bull. Eng. Geol. Environ.*, vol. 79, pp. 313-327, Jun. 2020.

[9] E. Grinzato, C. Bressan, S. Marinetti, P. Bison, and C. Bonacina, "Monitoring of the Scrovegni Chapel by IR thermography: Giotto at infrared," *Infrared Phys. Techn.*, vol. 43, no. 3-5, pp. 165-169, Jun. 2002.

[10] E. Kordatos, D. Exarchos, C. Stavrakos, A. Moropoulou, and T. Matikas, "Infrared thermographic inspection of murals and characterization of degradation in historic monuments," *Constr. Build. Mater.*, vol. 48, pp. 1261-1265, Nov. 2013.

[11] E. Grinzato, P. Bison, S. Marinetti, and V. Vavilov, "Nondestructive evaluation of delaminations in fresco plaster using transient infrared thermography," *Res. Nondestruct. Eval.*, vol. 5, no. 4, pp. 257-274, Dec. 1994.

[12] M. R. Clark, D. M. Mccann, and M. C. Forde, "Application of infrared thermography to the non-destructive testing of concrete and masonry bridges," *NDT E Int.*, vol. 36, no. 4, pp. 265-275, Jun. 2003.

[13] C. Lerma, Á. Mas, E. Gil, J. Vercher, and M. Torner, "Quantitative analysis procedure for building materials in historic buildings by applying infrared thermography," *Russ. J. Nondestr. Test.,* vol. 54, pp. 601-609, Nov. 2018.

[14] J. H. A. Rocha, Y. V. Póvoas, and C. F. Santos, "Detection of delaminations in sunlight-unexposed concrete elements of bridges using infrared thermography," *J. Nondestruct. Eval.*, vol. 38, pp. 1-12, Dec. 2019.

[15] M. Ishikawa, M. Tsukagoshi, H. Kasano, and H. Nishino, "Influence of composition and surface discoloration of concrete on active thermographic nondestructive inspection," *Measurement*, vol. 168, Jan. 2021, Art. no. 108395.

[16] M. Tortora, S. Sfarra, M. Chiarini, V. Daniele, G. Taglieri, and G. Cerichelli, "Non-destructive and micro-invasive testing techniques for characterizing materials, structures and restoration problems in mural paintings," *Appl. Surf. Sci.*, vol. 387, pp. 971-985, Nov. 2016.

[17] S. R. Wang, D. J. Li, C. L. Li, C. G. Zhang, and Y. B. Zhang, "Thermal radiation characteristics of stress evolution of a circular tunnel excavation under different confining pressures," *Tunn Under Sp Tech.,* vol. 78, pp. 76-83, Apr. 2018.

[18] Z. Liu, Q. Yao, B. Kong, and J. Yin, "Macro-micro mechanical properties of building sandstone under different thermal damage conditions and thermal stability evaluation using acoustic emission technology," *Constr. Build. Mater.*, vol. 246, Jun. 2020, Art. no. 118485.

[19] S. R. Wang, C. L. Li, D. J. Li, Y. B. Zhang, and P. Hagan, "Skewed pressure characteristics induced by step-by-step excavation of double-arch tunnel based on infrared thermography," *Teh. Vjesn.*, vol. 23, no. 3, pp. 827-833, Jun. 2016.

[20] R. Tomás, *et al.*, "Thermal effect of high temperatures on the physical and mechanical properties of a granite used in UNESCO World Heritage sites in north Portugal," *J. Build. Eng.*, vol. 43, Jun. 2021, Art. no. 102823.

[21] A. Kirimtat and O. Krejcar, "A review of infrared thermography for the investigation of building envelopes: Advances and prospects," *Energy Build.*, vol. 176, pp. 390-406, Oct. 2018.

[22] I. Garrido, S. Lagüela, S. Sfarra, F. Madruga, and P. Arias, "Automatic detection of moistures in different construction materials from thermographic images," *J. Therm. Anal. Calorim.*, vol. 138, pp. 1649-1668, Apr. 2019.

[23] J. L. Bodnar, J. C. Candoré, J. L. Nicolas, G. Szatanik, V. Detalle, and J. M. Vallet, "Stimulated infrared thermography applied to help restoring mural paintings," *NDT E Int.*, vol. 49, pp. 40-46, Jul. 2012.

[24] L. Collini, R. Garziera, and F. Mangiavacca, "Development, experimental validation and tuning of a contact-less technique for the health monitoring of antique frescoes," *NDT E Int.*, vol. 44, no. 2, pp. 152-157, Mar. 2011.

[25] X. Wu, X. Gao, K. Zhao, J. Liu, and X. Liu, "Abnormality of transient infrared temperature field (ITF) in the process of rock failure," *Chin. J. Rock Mech. Eng.*, vol. 35, pp. 1578-1594, Aug. 2016.

[26] C. Ge, L. Ye, S. R. Wang, H. B. Jia, S. T. Li, J. H. Yang, and S. Zhang, "Exploration method of stone statue based on nondestructive testing technology-taking Xinchang maitreya statue as an example," *J. Eng. Sci. Technol. Rev.*, vol. 12, no. 5, pp. 98-103, Nov. 2019.

[27] Y. F. Wang, S. R. Wang, F. Cui, and W. Wang, "Damage and frequency spectral characteristics of dry and saturated red sandstone subject to shear test, ". *Arab. J. Sci. Eng.*, vol. 48, no. 4, pp. 4609-4618, Jun. 2023

[28] F. Mercuri, U. Zammit, N. Orazi, S. Paoloni, M. Marinelli, and F. Scudieri, "Active infrared thermography applied to the investigation of art and historic artefacts," *J. Therm. Anal. Calorim.*, vol. 104, no. 2, pp. 475-485, May 2011.

[29] C. Meola, G. M. Carlomagno, and L. Giorleo, "The use of infrared thermography for materials characterization," *J. Mater. Process. Technol.*, vol. 155, pp. 1132-1137, Nov. 2004.

[30] J. Gong, Q. Q. Liu, S. R. Wang, Z. X. Wang, and C. L. Li, "Effects of modifiers on magnesium oxychloride cement doped with paper mill sludge", *DYNA*, vol. 98, no. 5, pp. 492-497, Oct. 2023.

[31] S. R. Wang, J. Q. Zhao, X. G. Wu, J. H. Yang, and Q. R. Wang, "Elastic properties and damage evolution analysis for lightweight shale ceramsite concrete, " *In. J. Appl. Mech.,* vol. 15, no. 5, May 2023, Art. no. 1950048.

[32] P. Xu, Y. H. Cui, J. F. Dai, S. R. Wang, M. X. Zhang, and Z. G. Hou, "Mechanical performance of texttile reinforced concrete containing steel fibers and basalt fibers dubjected to high temperatures," *Ceramics-Silikáty*, vol. 65, no. 3, pp. 263-272, Mar. 2021.

[33] G. M. Carlomagno and C. Meola, "Comparison between thermographic techniques for frescoes NDT," *NDT E Int.*, vol. 35, no. 8, pp. 559-565, Dec. 2002.

[34] L. Ye, M. Fang, Q. Pan, X. Xu, X. Wu, and S. Yuan, "Evaluation on weathering degree of limestone artifacts considering water absorption characteristics," *J. Eng. Sci. Tech. Rev.*, vol. 15, no. 5, pp. 1-8, Nov. 2022.

[35] N. Avdelidis and A. Moropoulou, "Applications of infrared thermography for the investigation of historic structures," *J. Cult. Herit.*, vol. 5, no. 1, pp. 119-127, Mar. 2004.

[36] A. C. Iñigo, *et al.*, "Colour and ultrasound propagation speed changes by different ageing of freezing/thawing and cooling/heating in granitic materials," *Cold Reg. Sci. Tech.*, vol. 85, pp. 71-78, Jan. 2013.

[37] F. Mercuri, N. Orazi, S. Paoloni, C. Cicero, and U. Zammit, "Pulsed thermography applied to the study of cultural heritage," *Appl. Sci.*, vol. 7, no. 10, Sep. 2017, Art. no. 1010.

[38] S. Liu, J. Wang, G. Chen, K. Meng, and Y. Zhang, "Thermal infrared precursor information of rock surface during failure considering different intermediate principal stresses," *Sustainability*, vol. 15, no. 11, May 2023, Art. no. 8877.

[39] F. Mercuri, C. Cicero, N. Orazi, S. Paoloni, M. Marinelli, and U. Zammit, "Infrared thermography applied to the study of cultural heritage," *Int. J. Thermophys.*, vol. 36, pp. 1189-1194, Jun. 2015.